4 Experimental method

The application of analogues to understand nature might be as old as man. One prominent example is the use of balls, instead of apples or cars to study the laws of conservation of either energy or momentum. The simplification of natural processes inherent in analogues enables the identification of the principles and the quantification of parameters that control nature and as such geodynamics. More specifically, mountain building is thought to depend on a multitude of parameters. Among the most important are deformation, erosion, sedimentation, and flexure, which may act on various time- and length-scales. Nonlinear feedback processes are therefore likely to occur. As noted earlier, considerable amount of research on mountain building by either physical or numerical simulations has been carried out during the last decades and the respective parameter space has been extensively explored. These simulation techniques require that the overwhelming wealth of possible parameters, as they emerge from field studies, is simplified and that those parameters are investigated in accordance to their expected importance within the geodynamic framework. It is emphasised here that such a simplification is implicitly based on several model assumptions outlined in previous chapters. The resulting setup, i. e., the kinematic boundary conditions, may guide not only the interpretation of experimentally derived results, but also one's perception of natural processes, which might finally evoke circular reasoning. However, a fixed reference frame in conjunction with known boundary conditions, which can only be inferred in nature, might also help to interpret experimentally derived results. Despite these epistemological challenges, physical forward modelling techniques such as sandbox simulations have been successfully applied and provided detailed insight into the parameters controlling mountain building: basal friction (Mulugeta, 1988; Liu et al., 1992; Calassou et al., 1993; Nieuwland and Walters, 1993; Luján et al., 2003); presence of several décollements (Kukowski et al., 2002; Couzens-Schultz et al., 2003); thickness of the incoming layer (Calassou et al., 1993; Nieuwland and Walters, 1993; Gutscher et al., 1998; Soto et al., 2002); backstop geometry and material (Davis et al., 1983; Malavieille, 1984; Byrne et al., 1988, 1993; Wang and Davis, 1996; Bonini et al., 1999; Storti et al., 2001); pore fluids (Cobbold et al., 2001); erosion and sedimentation (Merle and Abidi, 1995; Storti and McClay, 1995; Mugnier et al., 1997; Barrier et al., 2002; Persson et al., 2004; Hoth et al., 2006); topography (Dominguez et al., 1998; Marques and Cobbold, 2002; Del Castello et al., 2004); obliquity of convergence (Burbidge and Braun, 1998; Martinez et al., 2002; McClay et al., 2004; Hoffmann-Rothe et al., 2004). The above list does not claim to be complete.

The justification of the application of sandbox simulations to the brittle deforming part within orogenic wedges is derived from the fundamental observation that sand is characterised by similar mechanic properties as the upper brittle crust (section 4.1) and that brittle behaviour is scale-independent. The latter has been intuitively known from the earliest days of geology and led to the rule to always include a scale in drawings or maps. In later days, the scale independence has been more quantitatively shown by the Gutenberg-Richter-Law or by the length-displacement ratio of faults (e. g., Turcotte and Malamud, 2004). Also, a key prediction of the CCW concept, as outlined in section (3.3), is that the mechanics of mountain building are scale independent and can thus be understood while studying the mechanics of sand-wedges. Thus, the analysis of the spatio-temporal evolution of bivergent sand-wedges may provide predictions for natural observations which can be used in turn to constrain the former. In this study, emphasis is laid upon those predictions that are testable.

Two additional factors supported the use of 2D sandbox experiments. First, this method allows large magnitudes of convergence to be simulated. Second, a direct observation of strain localisation and fault propagation with a high temporal and spatial resolution, especially if monitoring techniques such as Particle Image Velocimetry (section 4.3) are applied, is possible.

Despite these advantages, sandbox simulations are like every other method associated with limitations, some with a more general and others with a more specific character. The former comprise the observation that subtle parameter variations, which can be easily explored with numerical simulations, are more difficult to test on their respective influence with sandbox simulations. However, the latter might provide trends, which can either be tested in numerical simulations or within field studies. Additionally, certain parameters such as erosion, sedimentation, fluid flow or phase transitions cannot be described or implemented in a physically correct way. In the case of erosion, sandbox experiments are "only" capable of simulating the effect, i. e., unloading of a structure, and not the process of erosion itself. Although, this limits the transfer of experimentally derived predictions to nature, we did not intend to rebuild a certain natural structure or geomorphologic feature and aimed at broader implications. Limitations, which are considered to be specific of the setup or the experimental implementation, are outlined were appropriate (section 4.2).

All sandbox simulations presented in this study were carried out at the Geodynamic Laboratory of the GFZ Potsdam, Germany. A short visit of the Tectonics Analogue Modelling Laboratory at the Vrije Universiteit Amsterdam, Netherlands was aimed at measuring the in-situ stress evolution in front of a propagating thrust. However, technical difficulties such as an insufficient shielding against external currents hindered success.

4.1 Physical properties of analogue materials

As indicated in the previous section, the knowledge of the physical properties of analogue materials is crucial for the justification of the sandbox simulation approach, to model upper crustal processes as well as the application of the CCW concept to laboratory sand-wedges. Since brittle behaviour is thought to be scale-invariant, the physical properties of the analogue materials were measured to compare experimental results with nature. Within this respect Hubbert (1937) noted that a change of the size of a given body is associated with a change of its physical properties. Therefore, sandbox-simulations do only unfold their full wealth of information if they are "properly" scaled with respect to their natural pendants.

The sand in this study, is derived from a Quaternary fluvio-glacial quartz sand deposit near Königslutter, Germany and shows a unimodal grain size distribution (Fig. 4.1). Grains are well to moderately rounded. Glass-beads ($300-400\,mm$) and mortar were used as well, whereas the latter is characterised by a unimodal distribution with a slight negative skewness (Fig. 4.1).

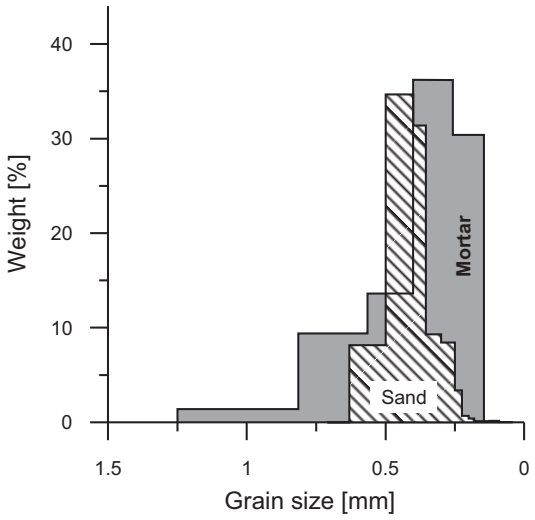

Figure 4.1: Grain size distributions of sand and mortar.

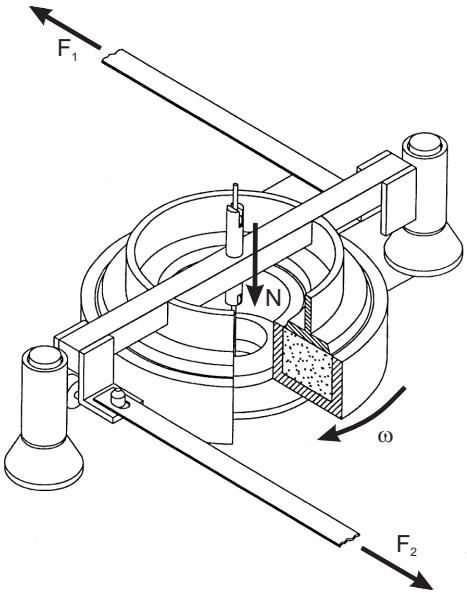

Figure 4.2: Ring-shear tester used to measure the mechanical properties of the analogue materials. N is normal load; ω is angular velocity; $F1$ and $F2$ are the measured shear forces. Modified after Schulze (1994).

A ring-shear tester (Schulze, 1994) was utilized to measure the internal and the basal mechanic properties of the above analogue materials (Fig. 4.2). To determine the internal mechanic properties, either sand, glass-beads or mortar was sieved into a shear box (Fig. 4.2), which was subsequently loaded with a range of normal loads ($1-12\,kg$). This range is similar to those normal loads, found in experiments. While the shear box rotated with a constant velocity, the associated shear force was measured. After an unloading phase during which the direction of rotation was reversed until the shear force dropped to zero, a new loading cycle was applied, i. e., the direction of rotation was again reversed. According to Byerlee (1978), this procedure allows the measurement of the frictional strength of the undeformed material (peak friction), the strength of the previously deformed material (static-stable friction) and the strength of active shear zones (dynamic-stable friction). A schematic stress-strain curve is shown in (Fig. 4.3). To asses the error associated with the above procedure, all measurements were carried out three times. The raw data in conjunction with REM images of the granular materials are provided in (Fig. 4.4) and are summarised in table (4.1).

With respect to the derivation of cohesion values from ring-shear measurements, Schellart (2000) demonstrated that for very small normal stresses ($<400\,Pa$) the Mohr envelope is characterised by a convex-outward shape which converges to a straight line with increasing normal stresses. Since the lowest normal stress applied during measurements at the GFZ Laboratory is $500\,Pa$, it is justified to derive the respective cohesion values from linear extrapolation of the Mohr envelope. Both the coefficient of internal friction and the cohesion obtained for the above materials agree with Lohrmann et al. (2003), who found that granular flow of sieved, dry quartz sand is characterised by a strain-dependent deformation behaviour with pre-failure strain hardening and post-failure strain softening and is therefore similar to the non-linear deformation behaviour of crustal rocks in the brittle field. Based on the S30T sand, Lohrmann et al. (2003) tested different grain-size distributions and found that the similarity between the mechanic properties of brittle upper-crustal rocks and the sand is highest for sieved sand with a grain-size distribution, ranging from $20-630\,mm$, which is therefore used in this study.

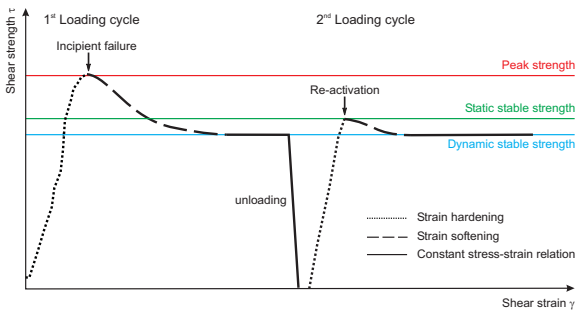

Figure 4.3: Characteristic stress-strain curve for the used sand as a function of angular shear (γ). Two loading cycles are shown. See text for explanations.

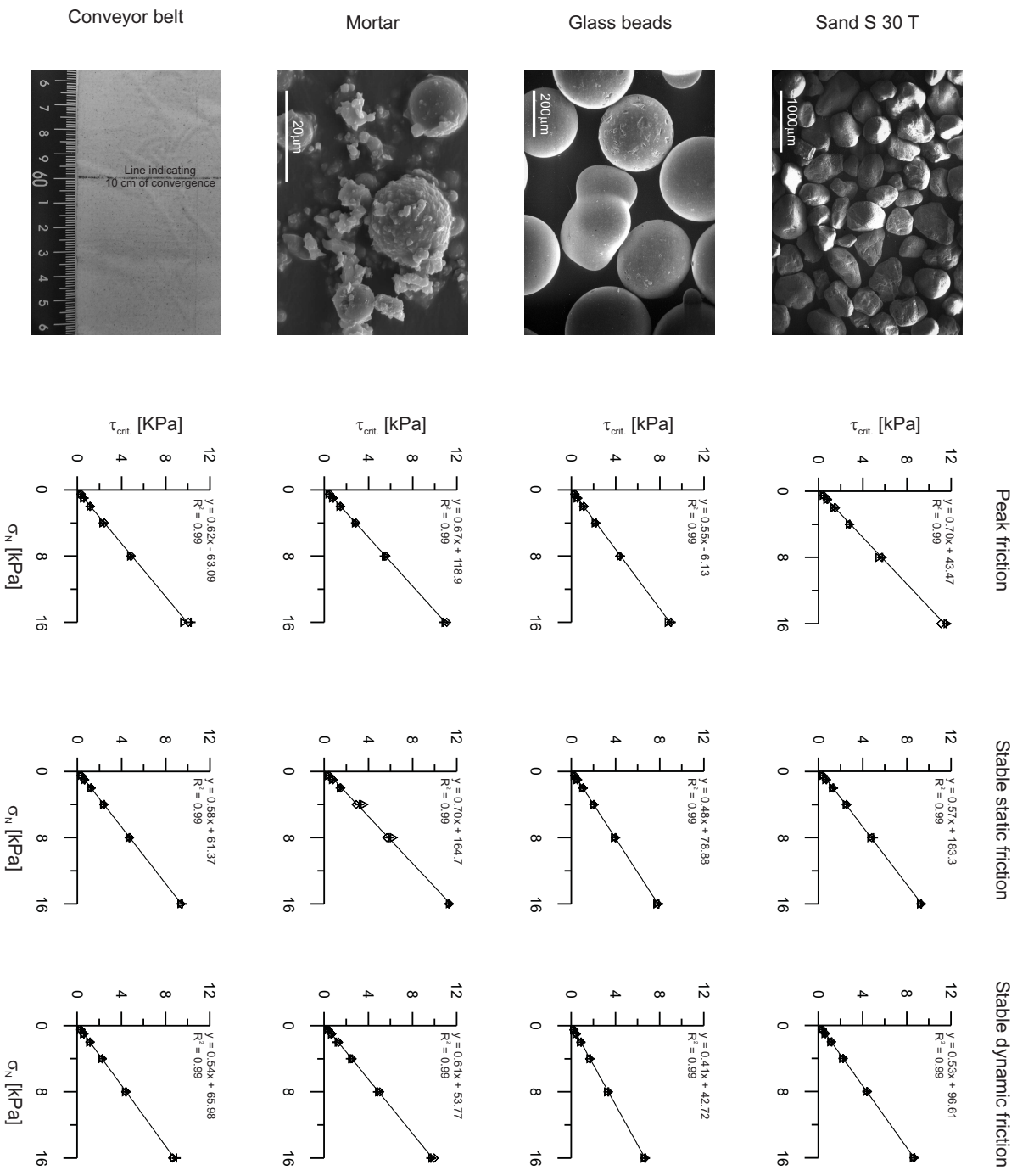

Figure 4.4: Results of ring-shear measurements. Shear stress τ is a function of the normal stress σ_N. Columns from left to right, if page is turned: REM images of granular analogue materials and photo from sandpaper, measured peak friction, stable static friction and stable dynamic friction. All measurements were repeated three-times. Respective angles of internal and basal friction as well as cohesion were derived from linear regression. Basal properties of the conveyor belt were measured with respect to the used sand. Note $10\,cm$ mark on conveyor belt, which was used to determine the duration of $10\,cm$ convergence.

Material	Type	Grainsize $[\mu m]$	Density $[g/cm^3]$	ϕ_{peak}* [°]	C_{peak} $[Pa]$	ϕ_{static}† [°]	C_{static} $[Pa]$	ϕ_{dyn}§ [°]	C_{dyn} $[Pa]$	Strain soft.‡ [%]
Sand	Internal	20 – 630	1.74	35.36	43.47	29.82	176.38	28.20	94.66	20.24
			±0.01	±0.34	±44.34	±0.19	±24.80	±0.05	±6.53	
Glass beads	Internal	300 – 400	1.59	29.14	-6.13	25.91	78.89	22.51	42.71	13.63
			±0.01	±0.14	±18.82	±0.09	±11.56	±0.04	±5.15	
Mortar	Internal	145 – 1250	1.82	34.09	118.89	35.18	164.71	31.38	53.77	7.95
			±0.03	±0.15	±20.54	±0.59	±77.27	±0.22	±28.95	
Sand paper	Basal	< 400	–	32.02	-63.09	30.34	61.37	28.62	65.98	–
				±0.32	±42.49	±0.07	±8.73	±0.15	±19.77	

Data are derived from ring shear tests. Internal properties were measured with sieved materials, basal properties were determined relative to sieved sand. Interpolation of the Mohr envelopes was used to calculate cohesion. The sand - S30T in industry standards - was washed and dried at high temperature by the mining company before delivery to the laboratory.
* Peak friction provides the strength of undeformed material.
† Static-stable friction provides the strength of previously deformed material.
§ Dynamic-stable friction provides the strength of active shear-zones (Byerlee, 1978).
‡ Strain softening is expresses as the percentage difference between peak friction and dynamic stable friction.

Table 4.1: Physical properties of analogue materials used in experiments

In the second measurement set, which followed the same procedure as the one described above, the basal properties of the sand with respect to the conveyor belt were determined. The latter is made of linen covered with an adhesive tape which in turn is sprinkled with sand ($20-400\,mm$), providing a high friction interface (Table 4.1). Based on these results, a geometric scaling factor, following Ramberg (1981) was calculated:

$$S = \frac{C\rho_m a}{C_m \rho g} \tag{4.1}$$

where the index m denotes the analogue model, S is the scaling factor, C is the cohesion, ρ is the density, g is the acceleration due to gravity in nature ($9.81\,m/s^2$) and a the one in the model. If all experiment are carried out under normal gravity conditions, equation (4.1) reduces to:

$$S = \frac{C\rho_m}{C_m \rho}. \tag{4.2}$$

Given that the density of sedimentary or upper crustal rocks ranges between $2000-3000\,kg/m^3$ (Landolt-Börnstein, vol. I "Physical properties of rocks" available at www.springerlink.com), analogue materials: $1500-1800\,kg/m^3$ and provided that the respective cohesion values are in the order of $0.7-105\,MPa$ (Landolt-Börnstein), analogue materials: $20-240\,Pa$. Consequently, S equates to a range ($10^3 - 10^6$), whereas 10^5 is the commonly used value. Consequently, $1\,cm$ in the model corresponds to $\sim 1\,km$ in nature. This scaling approach has been successfully used by a multitude of authors, among them Malavieille (1984), McClay (1996), Storti et al. (2000), Kukowski et al. (2002) and Del Castello et al. (2004). It is finally concluded that the theoretical considerations made in section (3.3), the measured mechanic properties of the analogue materials as well as the scale invariance of brittle failure, justify the approach of 2D sandbox experiments.

4.2 Experimental setup

Bivergent sand-wedges have been successfully simulated with two setups:

The mantle subduction model. Within an Eulerian reference frame, i. e., the material moves relative to the coordinate system, this model assumes that the mechanical energy delivered into an orogen is derived from the basal pull or drag of the subducting plate (Silver and Reed, 1988), since the crust is strongly coupled to the mantle lithosphere (Ellis et al., 1995; Ellis, 1996). This model was first

used in sandbox simulations by Malavieille (1984) and later adopted by Storti et al. (2000). These authors used the same material on both sides of the singularity. Within this scenario (Fig. 4.5a), upper plate material acts as a dynamic backstop sensu Kopp and Kukowski (2003). A rigid backstop (Fig. 4.5b) was used by Wang and Davis (1996), Bonini et al. (1999) and Storti et al. (2001) and their setups thus mediate between the mantle subduction and the indentor model, given below.

The indenter model assumes a strength contrast between the involved lithospheric plates and a weak coupling between the crust and the lithospheric mantle (Ellis et al., 1995; Ellis, 1996). Thus, the mechanical energy delivered into an orogen is derived from the push from the rear, which was also assumed in the CCW concept (Fig. 4.5c). This approach (Langrangian reference frame, i. e., the coordinate system moves with the material) was applied in sandbox simulations by Merle and Abidi (1995), Persson and Sokoutis (2002) and Persson et al. (2004).

Both types may provide end-member scenarios since Ellis (1996) pointed out that an orogen initially dominated by mantle subduction mechanics may, with continued convergence, evolve into an orogen dominated by indentor-style mechanics. If slab pull is considered as the most important force driving the plates (Conrad and Lithgow Bertelloni, 2004), the basal pull model was chosen. This bears also the advantage that the results drawn from this study can be easily compared with those from numerical simulations, which successfully simulated bivergent orogens with the basal pull approach (Batt and Braun, 1999; Willett, 1999; Beaumont et al., 2000; Pfiffner et al., 2000).

To study the most general case, collision of material with the same mechanical properties on both sides of the singularity was simulated (e. g., Storti et al., 2000). The respective upper plate material forms thus a dynamic backstop (Kopp and Kukowski, 2003). A strength contrast across the singularity was only simulated in one experiment.

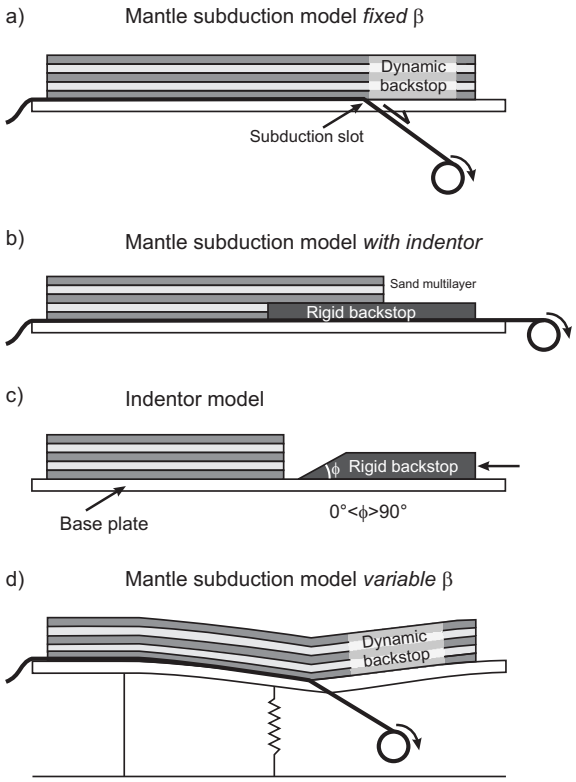

Figure 4.5: Summary of setups, which have been used to simulate bivergent sand-wedges. Two end-member models, i. e., the mantle subduction and the indentor type model have been put forward. (a) Mantle subduction model with a fixed β. (b) Mantle subduction model with an indentor. (c) Indentor model. (d) Mantle subduction model with a variable β as used in this study. See figure (4.6) for a technical sketch.

As indicated in chapter (1), the evolution of bivergent orogens is controlled by deformation, erosion/sedimentation, and flexure. To date, flexure has not been incorporated in sandbox-simulations, although it is commonly involved in numerical models (Willett, 1999; Pfiffner et al., 2000). Flexure is considered to be important, since the flexural rigidity of the involved plates controls the lateral and vertical distribution of tectonic loads (Allen and Allen, 2005), which in turn influences the spatial distribution of deformation (Boyer, 1995). Therefore, a new setup which allows for load-driven flexure was invented, i. e., the singularity migrates vertically and the dip angle β changes through time (Fig. 4.5d).

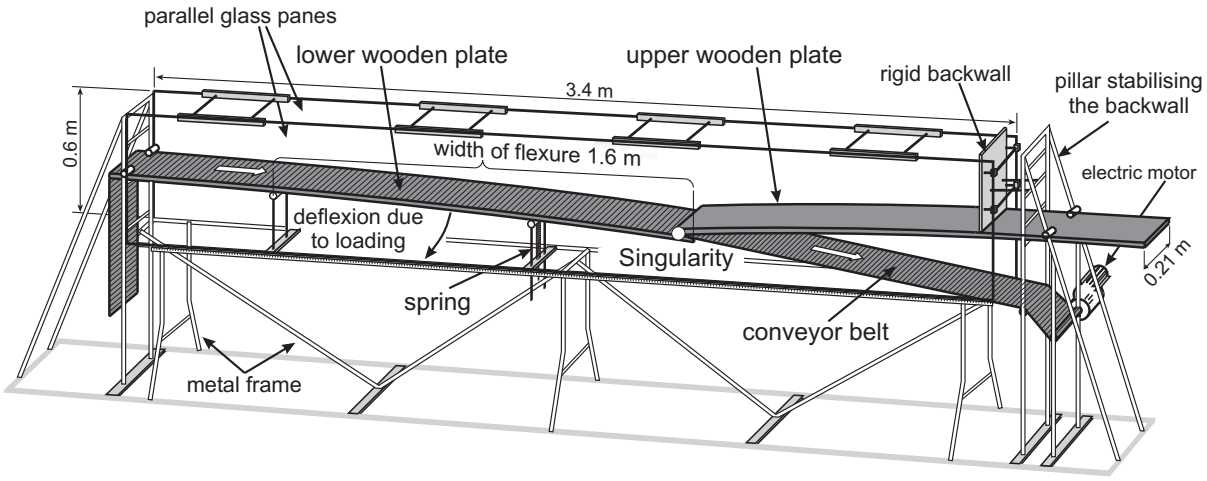

Figure 4.6: Technical sketch of sandbox, which allows for load-driven flexure.

The sandbox simulations were run in a glass-sided deformation apparatus with internal dimensions (length, width, height) of $340 \times 21 \times 60\,\mathrm{cm}$ (Fig. 4.6). It consists of an upper and a lower elastic wooden plate (referred to as upper and lower plate base), which overlap in the center. They are only fixed at their respective outward sides to allow for load-driven flexure. In order to minimise the influence of the boundary conditions imposed by the experimental device, the singularity is located sufficiently away from the rigid back-wall. The lower plate is supported by a spring to adjust its stiffness. Several test experiments were carried out to find an appropriate plate-spring combination, which ensures a constant increase of the dip angle β as well as a plausible magnitude for the latter. Thereby, four parameters were tested: (i) the distance between the free end and the point, where flexure is zero; (ii) the position of the spring with respect to the free end; (iii) the spring constant and (iv) the material of the plate bases. In order to find a plate-spring combination, which satisfies the above requirements, the free end of the lower plate was incrementally loaded with $2\,kg$ (maximum was $20\,kg$) and the vertical deflection was measured (Fig. 4.7). This was carried out for all parameter combinations listed in table (4.2). Finally, a plate-spring combination was chosen, for which β changes from $\sim 5^\circ$ to $\sim 7^\circ$ during experiments. The scaling factor between experimental and natural flexure is unknown because Young's modulus of the setup could not be determined.

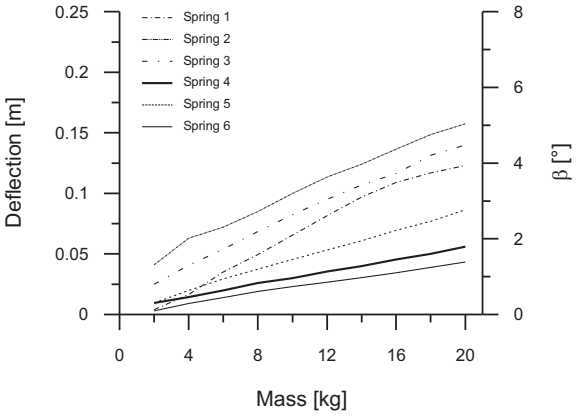

Figure 4.7: Load dependent deflection and basal dip β of lower plate. Length between the free and the point, where the deflection is zero, is $1.6\,m$, length between the free end and the spring is $0.3\,m$. Graph shows six springs, which differ with respect to their spring constants (see appendix). The above geometry together with spring 4 was chosen for experiment. During experiments load may reach up to $80\,kg$ and β changes correspondingly from about 5° to about 7°.

However, two disadvantages are associated with this new setup. First, the curvature of the plates hampers the preparation of the sand multilayer

Distance from free end and the point, where flexure is 0 [m]	Distance from spring to free end [m]				
	0.2	0.3	0.5	0.7	0.8
1.5	✓		✓	✓	
1.6		✓	✓		✓
1.9		✓	✓		✓

The thickness of the plywood was chosen to be $20.7\,mm$. A thicker or thinner plate would have provided either too little or too much deflection, respectively. The above parameter combinations were tested for six different springs. See appendix C for spring specifications.

Table 4.2: Parameters tested to find an appropriate plate-spring combination for the lower plate.

with a constant thickness, which is accounted for, by normalising all experimentally derived values with respect to the thickness of the incoming layer (H_0). Second, the glass panels had to be tangent to the base plates. Otherwise, sand grains would have fallen inbetween and would have resulted in a blurred profile view. It follows, that with respect to the above test experiments, the downward movement is retarded, whereas the upward movement is significantly delayed. Both features are not critical as long as the kinematic interpretation is not tightly linked with the magnitude of flexure, which is not intended and a net mass-gain of the bivergent sand-wedges is observed. The latter condition is satisfied for all, but one experiment. Additionally, reproducibility was successfully tested.

Lower-plate subduction and basal shear is simulated by a conveyor belt, which only covers the lower plate and is drawn by a motor ($\sim 9\,cm/min$) beneath the tip of the upper plate. In order to ensure a strong mechanical coupling between the conveyor belt and the sand layer, a sand paper with a grain size $< 0.4\,cm$ was chosen. The resulting basal friction (Table 4.1) is in the same range as published values for similar experimental devices (Wang and Davis, 1996; Kukowski et al., 2002). A lower basal friction would have resulted in a bivergent sand-wedge, which is wider and shows a lower α. In order to study the most general and simplest scenario, a $6\,cm$ thick sand layer covers the upper and lower plate base equally. We therefore did not account for (i) the variety of materials with differing frictional properties found in continental collision zones; (ii) the progressive foreland-ward decrease of the thickness of the sedimentary succession and (iii) inherited zones of weakness commonly found in orogenic forelands. The influence of the latter two factors on model results would have been a change in the spacing of thrusts (Bombolakis, 1986; Boyer, 1995; Hardy et al., 1998; Macedo and Marshak, 1999).

Most orogens, e. g., Pyrenees and European Alps, show a variety of possible detachment horizons, which can lead to orogen-scale frontal and basal accretion (e. g., Beaumont et al., 2000; Pfiffner et al., 2000). Such weak layers are simulated with dry glass-beads, which are characterised by a Mohr-Coulomb type rheology, but show significantly lower frictional properties as sand (Fig. 4.8, Table 4.1). In addition, Kukowski et al. (2002) found that an internal weak layer serves only as a detachment if its internal friction is significantly lower than the friction of the basal detachment. This imposed another constraint to use a high basal friction interface.

In order to promote frontal accretion within the retro-wedge, a basal glass-bead layer was placed above the upper plate base. Such an approach is in accordance with numerical simulations of bivergent wedges (e. g., Pfiffner et al., 2000).

Convergence is $\backsim 150\,cm$, i. e., $\sim 150\,km$ in nature and is therefore similar to medium-sized orogens like the European Alps or the Pyrenees. Thus, the applied kinematic boundary conditions resemble those in numerical and other physical simulations (Willett, 1999; Beaumont et al., 2000; Pfiffner et al., 2000; Storti et al., 2000;

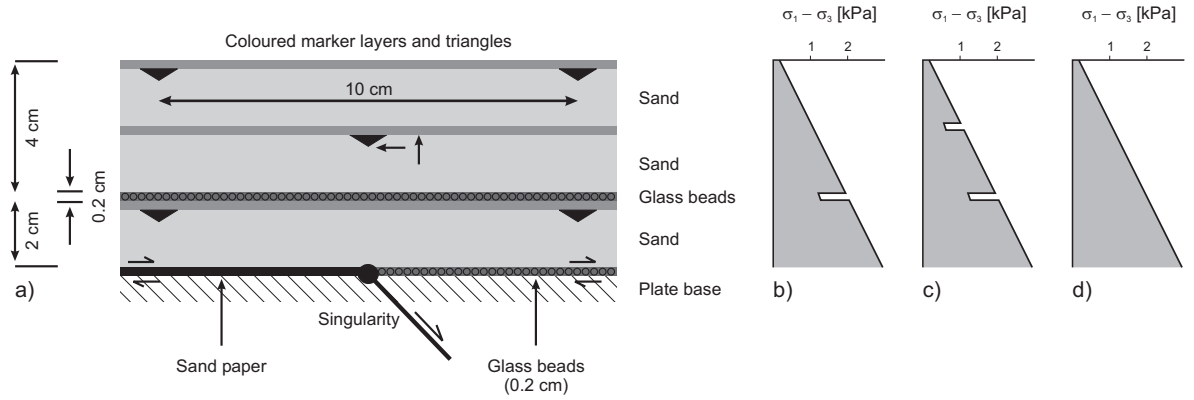

Figure 4.8: (a) Detailed mechanic stratigraphy with one internal glass-bead layer. The sand above is frontally, the sand below is basally accreted. (b) Calculated strength profile for mechanic stratigraphy in (a). (c) Calculated strength profile for a mechanic stratigraphy with two glass-bead layers. (d) Calculated strength profile for a mechanic stratigraphy with no glass-bead layer. (d) was used as the reference experiment for the 1^{st}, (a) as the reference experiment for the 2^{nd} experimental series. Strength profiles were calculated after Corti et al. (2003): $\sigma_1 - \sigma_3 = [2(C + \mu\rho gz)]/[(\mu^2 - 1)^{1/2} - \mu]$, where C is cohesion, μ is the coefficient of internal friction, ρ is the density, g is the acceleration due to gravity, and z is the depth.

Del Castello et al., 2004) and mimic the geometry of numerous published sections through small orogens (Beaumont et al., 2000; Pfiffner et al., 2000; Schäfer et al., 2000; Kummerow et al., 2004).

In erosion experiments, the sand wedge was allowed to produce an initial topography during the first 40 *cm* of convergence before incremental erosion was simulated. The convergence prior to erosion ensured that the bivergent sand-wedge was fully established. In order to unequivocally detect the influence of the location and the mode of erosion on the kinematics of bivergent sand-wedges, five simplifying assumptions were made:

i. Either the pro- or the retro-wedge is eroded.

ii. To ensure comparison between experiments, erosion was simulated at a constant interval (10 *cm* of convergence). The reader is referred to section (6.3.2) for a detailed discussion on the continuous deformation versus discrete erosion challenge.

iii. Both erosion modes were investigated separately despite the observation that most natural bivergent orogens undergo distributed and focused erosion at the same time.

iv. During experiments all eroded material left the model system and sedimentation either in the foreland or in piggy-back basins was neglected. This procedure is justified by the following observations: Deposition within foreland basins is highly variable along-strike. Morris et al. (1998) showed that along-strike variations in sediment discharge, calculated from apatite fission track ages, may reach up to 500 % between drainage basins in the Pyrenees. They further pointed out that temporal variations of sediment discharge from individual drainage basins are greater than 300 %. A similar observation was made by Kuhlemann (2000) for the European Alps. Based on mass budget calculations, he pointed out that since the Oligocene, the temporal variations of sediment supply are in the order of 550 % for the Swiss and Western Alps and up to 1000 % for the Eastern Alps. His data do also suggest that only $\sim$ 50 % of the debris derived from the European Alps were deposited in the peripheral foreland basins. The remaining $\sim$ 50 % were shed either into the Gulf of Lyon (Rhône fan), the Adriatic and Ionian basins or in the Pan-

nonian basin. Results from balanced crustal-scale cross-sections from the Eastern Pyrenees (Vergés et al., 1995) and the Swiss Alps (Adrian Pfiffner pers. com., (2003)) suggest that one half to two thirds of the eroded material was either shed into the Atlantic during middle Lutetian to late Oligocene times (Eastern Pyrenees) or into the Gulf of Lyon (Swiss Alps), which agrees thus well with Kuhlemann (2000).

v. The key assumption made for the experiments involving erosion is that erosion rate is positively correlated with elevation (chapter 2). Accordingly, distributed erosion is simulated as follows. Erosion increases linearly from the toe of either the pro- or the retro-wedge towards the top of the bivergent sand-wedge, where it reaches its maximum of $1\,cm$ per $10\,cm$ of convergence (Fig. 4.9). Erosion in the focused mode reaches its maximum of $1\,cm$ per $10\,cm$ of convergence at the middle of either the pro- or the retro-wedge slope and decreased toward zero at the respective tops and toes.

In order to compare the magnitude of erosion with natural examples we calculated the erosion efficiency parameter $r = v_e/v_c$, where v_e is the erosion rate, i. e., $1\,cm$ of erosion per $10\,cm$ of convergence and v_c is the convergence velocity, i. e., $10\,cm$ of material input per $10\,cm$ of convergence. It is highlighted here that the velocity with which the conveyor belt is drawn ($\sim 9\,cm/min$) is of no importance for the above calculation since deformation of a Mohr-Coulomb material like sand is not time-dependent. We further assume that the instantaneous removal of sand, as simulated, reflects a continuous removal of $1\,cm$ per $10\,cm$ of convergence. The resulting value r = 0.1 is thus well in the range of natural values obtained from currently deforming orogenic wedges such as Taiwan: 0.03 – 0.18 (Dadson et al., 2003), New Zealand: 0.5 – 1.3 (Hovius et al., 1997; Koons et al., 2003), Southern Alaska: 0.02 – 0.94 (Meigs and Sauber, 2000), and the Himalayas: 0.07 – 0.25 (Bilham et al., 1997; Thiede et al., 2004). It is emphasised again, that it was not intended to accurately simulate the process of either distributed or focused erosion. Instead, the differing magnitudinal distributions across orogenic strike of both erosion modes, as they emerge from field studies (chapter 2), were used.

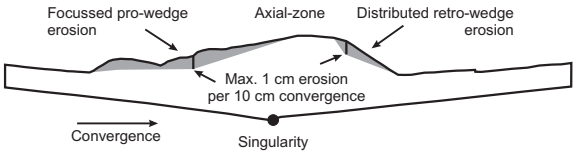

Figure 4.9: Distribution of incremental erosion, either distributed or focused.

Finally, during all experiments either with or without erosion, the internal and basal mechanic properties were held constant. Examination of both cross sections during and after each experiment revealed that the plane strain assumption is valid. Reproducibility is justified by the repetition of experiments and the comparison of emerging trends and mutual relations of different data sets such as the propagation of deformation, particle paths and the amount of erosion, with the ones derived from similar experimental series.

4.3 Data acquisition and processing with Particle Image Velocimetry

Particle Image Velocimetry (PIV) is based on an adaptive cross correlation algorithm, which compares successive images and enables thus the calculation of the incremental displacement field within sand-wedges, the corresponding horizontal and vertical components as well as the incremental shear-strain (Adam et al., 2005).

The PIV system at the Geodynamic Laboratory of the GFZ Potsdam, Germany is made up of two high speed, digital cameras (2000×2000 pixels), which were used to monitor all experiments. The

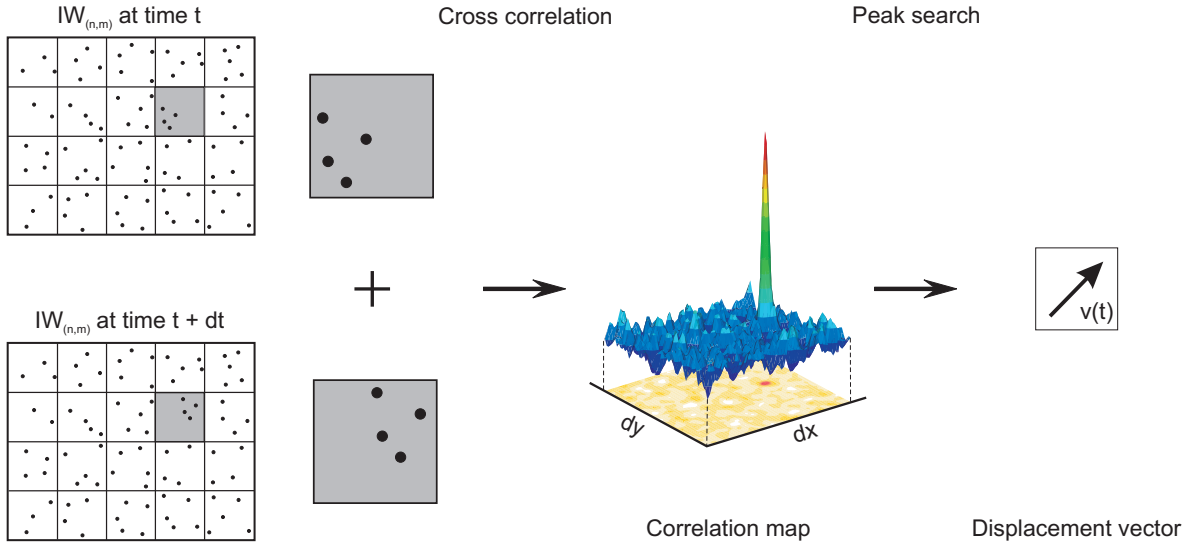

Figure 4.10: PIV workflow. Every image is divided into interrogation windows (IW), which are associated with an intensity value. During cross-correlation $IW_{(n,m)}$ at time $t+dt$ is shifted incrementally by dx and dy with respect to $IW_{(n,m)}$ at time t. For each position a correlation coefficient between both intensities is calculated with Fast Fourier Transformation. Respective results are stored in a correlation map. The coordinates of the maximum correlation peak reveal the most likely position of the local displacement vector to match the pattern of $IW_{(n,m)}$ at $t+dt$ to $IW_{(n,m)}$ at t. Modified after LaVision Göttingen.

resolution of both cameras is sufficiently high to image individual sand-grains. Images were taken every $2\,s$ during experiments with erosion and with one exception at every $1\,s$ for experiments without erosion. The higher temporal resolution of the latter was chosen to ease comparison with other standard experiments carried out within the laboratory. The software DaVis developed by LaVision GmbH, Göttingen, Germany was used to operate both digital cameras and to finally process and analyse the respective images. Acquisition and processing of the images involves four steps:

i. Prior to image acquisition both cameras are calibrated and a mapping function is calculated to correct the images for distortions, resulting from the view angle of the cameras.

ii. According to the mapping function the images are corrected during acquisition.

iii. Both images are stitched together and the scale of the images [pixel] is converted to millimeter using again the mapping function.

iv. Based on an adaptive cross correlation algorithm, successive images are compared and the incremental displacement field is calculated as explained below (Fig. 4.10).

Cross correlation of successive images (image 1 at time t, image 2 at time $t+dt$) involves the division of each image into interrogation windows (IW 1, IW 2), which were assigned an intensity value. With respect to IW 1, the second interrogation window is now shifted incrementally by dx and dy in both x and y direction. For each position a correlation between both intensities is calculated with Fast Fourier Transformation and results are stored in a correlation map (Fig. 4.10). The coordinates of the maximum correlation peak reveal the most likely position of the local displacement vector of this sub-sample to match the pattern of IW 1 to IW 2 (Adam et al., 2005). It follows that the local displacement vector is a spatial average for the entire interrogation window. The corresponding spatial resolution can be improved by using adaptive multi-pass correlation

(Flow Master© Manual by LaVision; Adam et al. (2005) and references therein). This algorithm calculates a vector field based on a large interrogation window size. In the next step the size of the interrogation window is half the previous size and the first vector field is now used as a reference. Thus, the shift of the interrogation windows is adaptively improved and the calculated vectors become more reliable. Accuracy of the displacement measurement is $\sim 0.5\,mm$ and is thus equal to $\sim 50\,m$ in nature (Adam et al., 2005).

The incremental vector field forms the basis for the calculation of its derivatives such as its horizontal and vertical components and the associated components of the strain tensor, e. g., e_{xy}. Thereby, e_{xy} denotes the change of the x-component of the velocity vector in the y-direction and is thus referred to as horizontal shear strain. However, a complete description of the state of plane strain within the bivergent sand-wedges would require the calculation and analysis of horizontal and vertical shortening (e_{xx} and e_{yy}). Given that the strain field in orogenic wedges results from the lateral shortening and vertical thickening (Ranalli, 1995), e_{xy} is thus considered as a good measure of bivergent wedge deformation.

4.4 Data mining and its limitations

The digital images recorded by PIV provide an excellent possibility to extract time series data for several geometric features such as the propagation of deformation, the height above the singularity or the length of thrusts (Fig. 4.11). These geometric features are commonly thought to be indicative for the kinematic evolution of bivergent sand-wedges. They also allow a quantitative comparison between experiments and may finally provide a link to data from natural bivergent orogens.

All geometric data derived from PIV analysis were normalised with respect to H_0, the height of the undeformed multilayer, to account for slight variations in its thickness. These geometric data were taken at every fifth image which corresponds to a convergence interval of $1.5\,cm$. Since the geometric data were collected in the time domain $[s]$, they had to be transferred to the convergence domain $[cm]$ to ensure comparability between experiments. The respective conversion procedure bears some error as indicated below. During experiments marks drawn at every $10\,cm$ on the conveyor belt passed an external reference frame, while the corresponding PIV image number, which provides the time in $[s]$ was taken. Although the motor runs at a constant velocity ($9\,cm/min$), the velocity of the conveyor belt increases with time, as the radius of the engine shaft plus the winded conveyor belt increases. However, significant deviations from this linear trend occurred (Fig. 4.12). As a first-order approach the linear increase was used to convert time to convergence and the associated error is $\sim 5\,\%$. The accuracy of measured lengths within PIV images is in the order of four to six pixels, which are $\sim 2-3\,mm$.

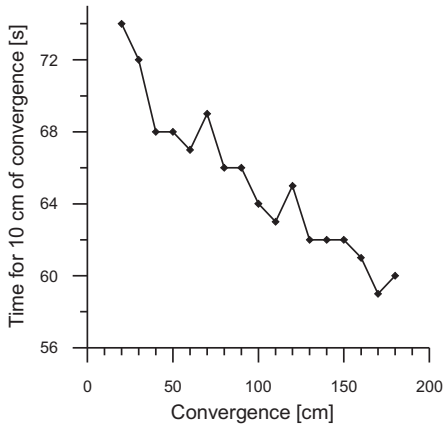

Figure 4.12: Change of the duration of $10\,cm$ of convergence during the reference experiment. Deviations from linear decrease (see text) may either result from human error or from wedge kinematics, but no relation could be established.

In order to elucidate the spatio-temporal evolution of deformation within, and of the associated surface uplift of a bivergent wedge, three new display-types were invented. To ensure successful communication the reader is provided with a how to read guide:

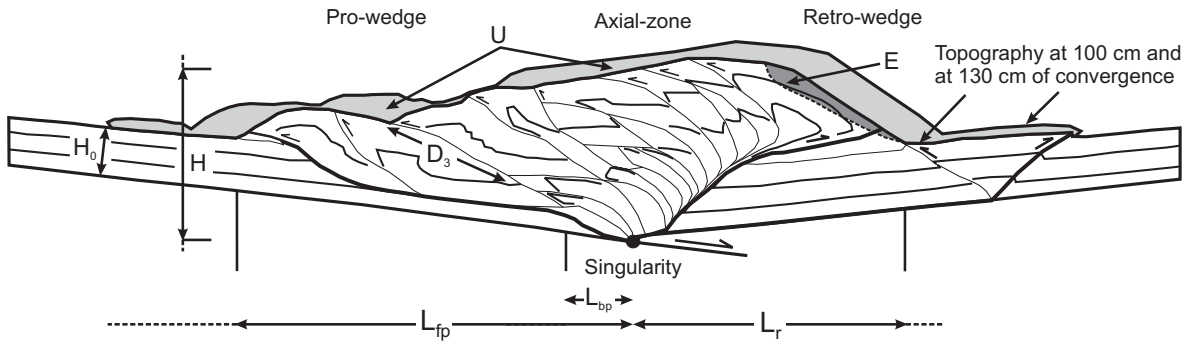

Figure 4.11: Measured parameters, which describe bivergent wedge evolution. (i) Propagation of the deformation front of frontal accretion in the pro-wedge [L_{fp}], (ii) Propagation of the deformation front of basal accretion in the pro-wedge [L_{bp}], (iii) Topographic height above the singularity [H], (iv) propagation of the deformation front of the retro-wedge [L_r], (v) Length of individual thrusts [$D_{1...8}$] , (vi) Erosion [E] and (vii) Incremental surface uplift [U]. Index p relates to the pro-wedge, index r to the retro-wedge, index f to frontal accretion and index b to basal accretion. H_0 is the height of the undeformed multilayer. All geometric features are normalised with respect to H_0 to account for slight variations in the thickness of the multilayer.

Topographic envelopes. Every pixel in a PIV image is assigned with an intensity value (counts). Pixels of the background or the setup are set to 0, pixels of the sand-wedge are set to 1 count. This leads to a black (background and setup) and white (sand-wedge) image, which forms the basis for all later calculations (Fig. 4.13a, b). At this stage two sources of error may occur. First, the PIV cameras have a perspective view on the sand wedge, i. e., they image the third dimension, which can result in an overestimation of the wedge area. Second, the definition of background and sand wedge is ambiguous with respect to the number of counts, since a certain cut off had to be chosen. This may also lead to an over- or an underestimation of the wedge area. The respective black and white image is exported as a bitmap (another source of error) and is finally automatically digitised. Especially the latter procedure can lead to an over- or an underestimation of the wedge area. Thus, some care should be taken while analysing the topographic envelopes (Fig. 4.13c). Nevertheless, they show first and second order features, thought to be valid [see section 5.1] but may have some inconsistencies, especially with respect to the thickness of the incoming layer. Topographic envelopes were generated at every 10 *cm* of convergence.

*Incremental Surface Uplift (*ISU*) maps.* To calculate ISU , an increment is 10 *cm* of convergence, the area of a sand wedge at time t is subtracted from the area of a sand wedge at time t + 10 *cm* of convergence. This results in secondary black and white image, which shows the spatial distribution of ISU (Fig. 4.13d). Its magnitude is measured at the scale of a pixel and an uplift curve is generated. Finally, all uplift curves are grided and displayed as a map, which indicates the spatial and temporal distribution of ISU in an Eulerian reference frame (Fig. 4.13e, f). The sources of error associated with ISU maps are similar to the ones determined during the derivation of the topographic envelopes. But again, ISU maps are thought to indicate first and second order phenomenons. Therefore, subtle variations of ISU were not interpreted. Nevertheless, ISU maps provide a wealth of information and can be read at least in two ways. Timelines (horizontal) indicate the spatial distribution of ISU for a certain stage during wedge evolution. Location lines (vertical) provide the change of ISU through time at a given position. The spatial resolution of ISU maps depends on the mapping function, but is generally around 0.5 *mm*. The temporal resolution is 10 *cm* of convergence. Narrower intervals have not provided more information.

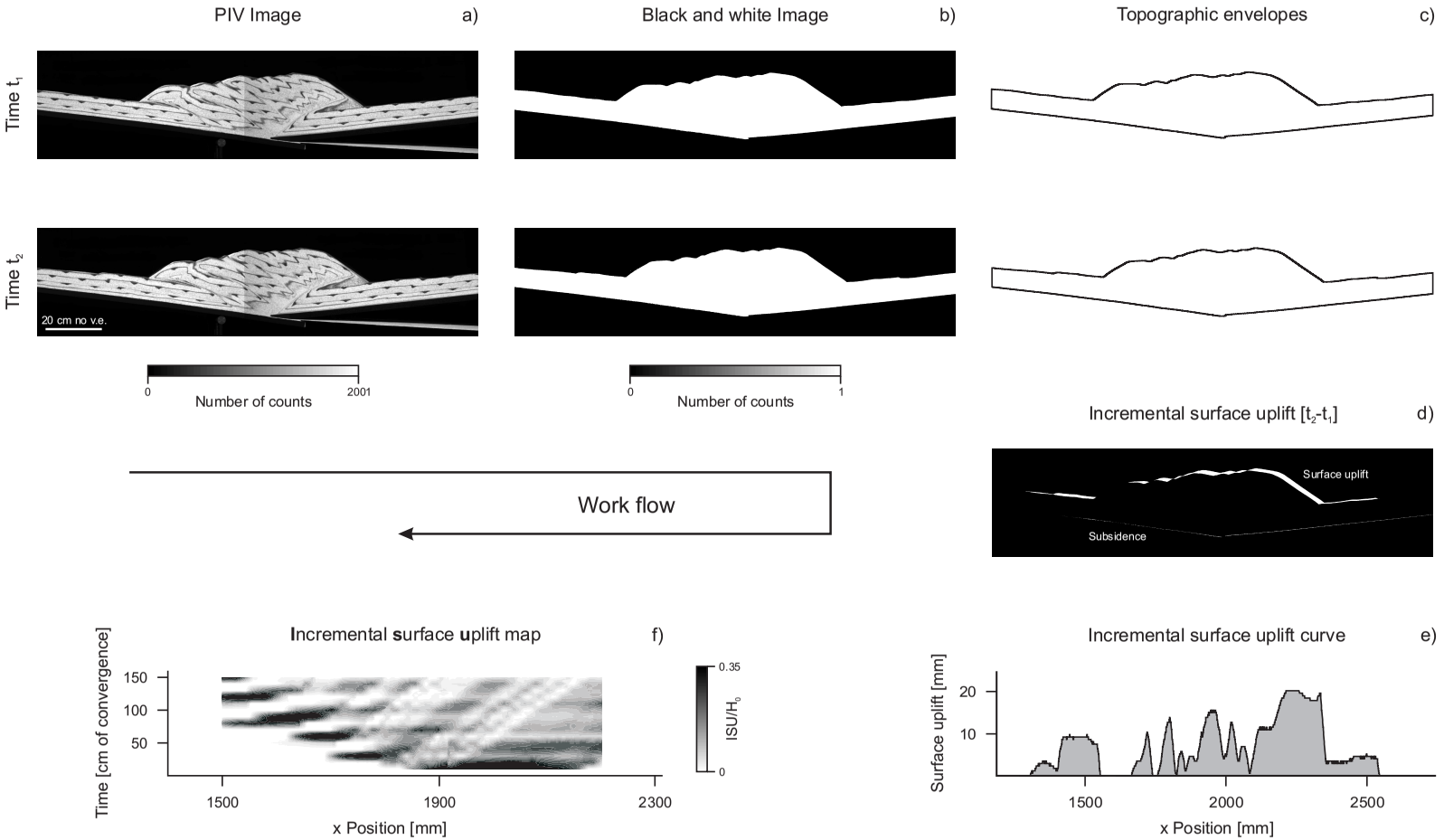

Figure 4.13: Generation of topographic envelopes and of ISU maps. (a) Original PIV images. (b) Converted PIV images. (c) Topographic envelopes of bivergent sand-wedge at t_1 and t_2 derived from automatic digitisation of (b). (d) Subtraction of converted PIV images (b) results in incremental surface uplift. Increments correspond to $10\,cm$ of convergence. (e) Incremental surface uplift is measured and displayed as a curve. (f) Map display of all incremental surface uplift curves.

Evolution of Deformation Maps (EDM). The incorporation of PIV into sandbox simulations resulted in an overwhelming wealth of data with respect to the spatio-temporal distribution of incremental strain. Therefore, the need emerged to display these data in a way that facilitates the detection of trends or patterns. In a first step the scalar of e_{xy} was extracted. In a second step, e_{xy} is measured along a profile parallel to the base plates (Fig. 4.14a). A likewise processing of all images results in e_{xy} profiles, which are finally displayed (Fig. 4.14b). The EDM provides thus the spatio-temporal distribution of e_{xy} in an Eulerian reference frame and allows the analysis of strain transfer patterns. Since material moves through the profile line and the angle between the latter and the ramp segments is not constant due to continued accretion and flexure, several EDM were calculated for different positions of the profile line. The resulting e_{xy} pattern was similar, although the magnitudes differed. Note that the position of the profile line determines the visibility of the backthrusts associated with the major thrust imbricates.

Strain histories for individual thrusts. First, the finite Lagrangian e_{xy} after 140 cm of convergence is calculated (Fig. 4.4a). Then, all particles and their associated finite e_{xy} magnitude are restored back to their original position prior to convergence (Fig. 4.4b). Similar to the procedure described above the scalar of e_{xy} is extracted from every image and e_{xy} is measured along a profile line, parallel to the base plates. The resulting map indicates thus the accumulation of finite strain through time for every position along the profile line (Fig. 4.4c). Now, the finite e_{xy} history is derived for a point, located within a ramp segment through a vertical profile (Fig. 4.4d). If this is done for all ramp segments, strain transfer patterns can be identified. They compare well with the ones recognised in the EDM. In the final stage incremental e_{xy} histories for a certain point located within a ramp segment are derived from the finite ones (Fig. 4.4d, e).

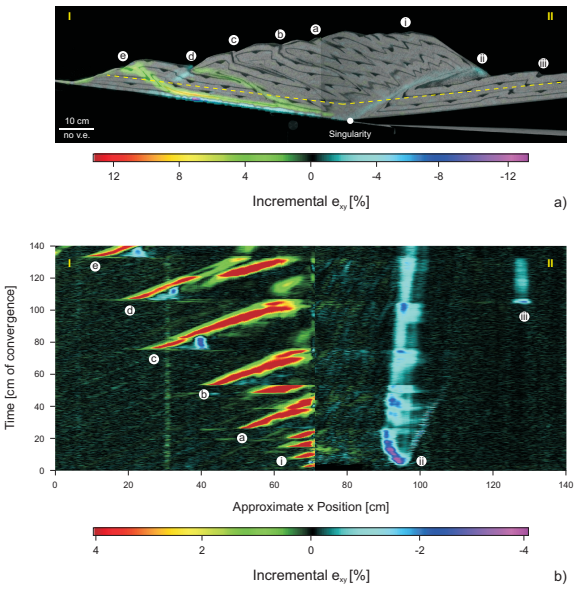

Figure 4.14: Derivation of EDM. Incremental e_{xy} is extracted along profile I - II (a) for every image and is finally displayed as a map (b). Labels ⓐ to ⓔ refer to forethrusts within the pro-wedge. ⓘ denotes the pro-shear of the initial pop-up, ⓘⓘ the respective retro-shear and ⓘⓘⓘ the accretion within the retro-wedge. Only the approximate x position is given, since the raw data are enlarged during extraction from PIV.

Finally, four conventions are made. The term *pro-shear* is used for all shear zones, which dip towards the upper plate, whereas shear zones with *retro-shear* dip towards the lower plate. In e_{xy} images, the former is coloured in green to red, the latter in blue to purple. The term *retro shear-zone* is taken only for the shear zone bounding the retro-side of the initial pop up (section 3.1). The term *incremental* refers to a convergence interval of 10 cm, if used to describe the topographic evolution of the bivergent wedges. If however *incremental* is used in conjunction with strain information, than this term describes the time between two successive PIV images.

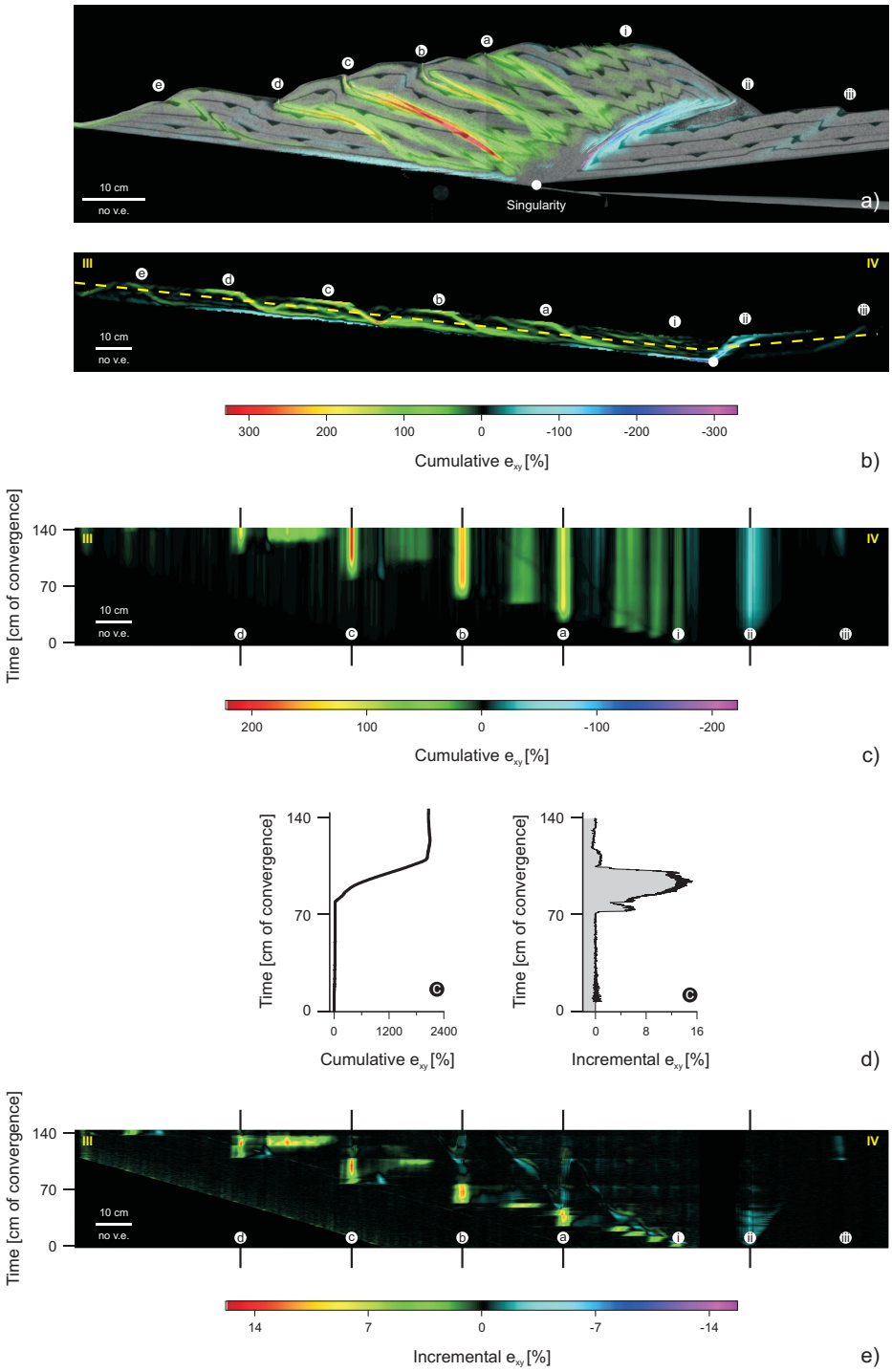

Figure 4.15: Derivation of e_{xy} profiles for ramp segments of the forethrusts and the retro-shear zone. (a) Finite e_{xy}, i. e., after 140 cm of convergence. Annotations are the same as in figure (4.14). (b) Restoration of original particle position. (c) Cumulative e_{xy} values are extracted from profile III – IV in (b) for every image and are displayed as a map. (d) Extraction of cumulative e_{xy} values from a vertical profile. (e) Shows the incremental e_{xy} accumulation for each location along profile III – IV in (b). Vertical profile in (e) provides e_{xy} history of points within ramp segments of the forethrusts and is shown in (d).